Computers and Geosciences 118 (2018) 100–108

Contents lists available at ScienceDirect

Computers and Geosciences

journal homepage: www.elsevier.com/locate/cageo

Research paper

E-Wave software: EBSD-based dynamic wave propagation model for studying seismic anisotropy

Xin Zhong[a,*], Marcel Frehner[b]

[a] Physics of Geological Processes (PGP), The Njord Center, University of Oslo, Postboks 1048 Blindern, Oslo, Norway
[b] Department of Earth Sciences, ETH Zurich, Sonneggstrasse 5, 8092, Zurich, Switzerland

ARTICLE INFO

Keywords:
Wave propagation
Seismic anisotropy
EBSD
Finite difference method

ABSTRACT

The study of seismic anisotropy has benefited from the wide application of the electron backscatter diffraction (EBSD) technique that provides complete information on the crystallographic and shape preferred orientations in 2D sections. Classical effective medium theory statistically approximates the seismic anisotropy based on the crystallographic preferred orientation, but the shape preferred orientation is often idealized as e.g. parallel layering or oriented inclusions. Due to higher demands in precisely quantifying seismic anisotropy in natural rocks and taking full advantage of the EBSD technique, dynamic wave propagation methods have received broad attention. This paper presents the MATLAB program *E*-Wave based on a novel approach to directly use EBSD data for 2D numerical wave propagation simulation. The complete mechanical formulation and numerical benchmarks with simple model setups are presented. The *E*-Wave program allows straightforward EBSD data import, finite-difference simulations with one-button click, and automatic result analysis. The *E*-Wave program can be a helpful and independent tool in future works to shed light on the relationship between microstructures and seismic anisotropy, and contribute from the modelling perspective to studies in seismology, geodynamics and rock physics.

1. Introduction

Natural minerals are heterogeneously distributed in rocks and often elastically anisotropic, which results in the velocity of seismic waves to be macroscopically distinct along different propagation directions. This property called seismic anisotropy is typically related to and controlled by the deformation of rocks. For example, seismic anisotropy offers a unique opportunity to investigate the past and present-day flow direction in the mantle and crust (e.g. Kneller and van Keken, 2007; Long and Becker, 2010; Lloyd et al., 2011; Skemer and Hansen, 2016; Almqvist and Mainprice, 2017). Seismic anisotropy is caused by two main reasons: 1) the crystallographic preferred orientation (CPO) of the anisotropic crystals and 2) the shape preferred orientation (SPO) of irregularly aligned minerals with different geometry (Mainprice, 2015). Classical quantitative methods to study seismic anisotropy involve different ways to statistically average the elastic moduli, e.g. the frequently used Voigt and Reuss bounds (e.g. Mavko et al., 2009). To this end, the effective medium theory is used assuming that either the elastic strain (Voigt bound) or stress (Reuss bound) is homogeneous in space. The arithmetic average of Voigt and Reuss bounds (Hill average) is often taken to approximate the seismic anisotropy (Hill, 1952). Other averaging methods are established for particular material geometries, for example the Backus solution for periodically stacked (transversely) isotropic layers (Backus, 1962; Schoenberg and Muirt, 1989), or the Hashin–Shtrikman bounds for oriented spherical/elliptical inclusions in a homogeneous matrix (e.g. Willis, 1977; Brown, 2015). However, most statistical averaging approaches focus on the effect of CPO while the SPO is idealized (e.g. parallel layers, oriented inclusions). It has been emphasized that real rocks are heterogeneous and may contain irregularly shaped fractures or inclusions that are filled with different materials (e.g. fluid, glass, melt) (Anderson et al., 1974; Schoenberg, 1995). These heterogeneities are not easily captured by effective medium theories, and pose difficulties when evaluating seismic anisotropy as a function of both crystallographic and shape preferred orientations. Different from the effective medium theory, the asymptotic expansion homogenization (AEH) finite-element (FE) method takes into account the microfabric characteristics of CPO and elastic grain interactions by calculating the bulk elastic moduli considering grain shape distributions (e.g. Naus-Thijssen et al., 2011; Vel et al., 2016). However, as no seismic wave propagates through the FE mesh, the effect of elastic scattering at grain boundaries is not evaluated. The elastic scattering effect may become significant when the ultrasonic

* Corresponding author. Sem Sælands vei 24 Fysikkbygningen, 0371, Oslo, Norway.
E-mail address: xinzhong0708@gmail.com (X. Zhong).

https://doi.org/10.1016/j.cageo.2018.05.015
Received 8 October 2017; Received in revised form 28 May 2018; Accepted 31 May 2018
Available online 04 June 2018
0098-3004/

wavelength is similar or shorter than the grain size, and is not easily evaluated with many modelling techniques (Arntsen, 2007).

Electron backscatter diffraction (EBSD) has become a standard technique to map mineral phases, (sub)-grain boundaries, and crystallographic orientations in a 2D section (e.g. Adams et al., 1993; Bascou et al., 2001; Humphreys, 2001; Lloyd et al., 2011; Austrheim et al., 2017; Dunkel et al., 2017). A novel numerical model has been developed to use the measured CPO and SPO information for modelling dynamic wave propagation (Zhong et al., 2014). This approach uses the digital EBSD data to generate a numerical finite-element grid and simulates the dynamic propagation of seismic waves through the measured 2D EBSD-section. Recently, this novel approach has received attention because of the greater demand in precisely quantifying seismic anisotropy and the prevalent use of the EBSD technique (Skemer and Hansen, 2016; Almqvist and Mainprice, 2017). However, the work in Zhong et al. (2014) focuses on various applications combining the EBSD technique, laboratory ultrasonic transmission experiments, and the numerical solutions of seismic anisotropy in a case study of one particular rock type (i.e., Finero peridotite, Italy). Unfortunately, this EBSD-based dynamic wave propagation model is not readily used in relevant studies due to the complications in tensorial rotations, EBSD data import and programming with the finite-element method. Therefore, this paper presents a MATLAB-based GUI program (*E*-Wave) that allows easy EBSD data import, numerical simulations based on a simpler finite-difference (FD) method, and processing/visualization of numerical solutions. The mechanical formulation and background for the EBSD-based wave propagation model are provided and the *E*-Wave program is benchmarked with analytical solutions in two simple model setups. The ultimate goal is to present *E*-Wave as a convenient and robust program for EBSD users to take the full advantage of the EBSD-technique in studying seismic anisotropy.

2. Methods

The wave propagation model is formulated with the momentum balance equations and the elastic constitutive relation (Hooke's law). A 4th order tensor rotation is introduced to rotate the stiffness tensor from the sample reference frame into the crystal reference frame. The staggered-grid FD-technique in space is used to solve the system of equations with an explicit FD time-marching technique.

2.1. Governing physics

The generalized linear Hooke's law is expressed using the Voigt notation:

$$\begin{bmatrix} \sigma_{xx} \\ \sigma_{yy} \\ \sigma_{zz} \\ \sigma_{yz} \\ \sigma_{xz} \\ \sigma_{xy} \end{bmatrix} = \begin{bmatrix} C_{11} & C_{12} & C_{13} & C_{14} & C_{15} & C_{16} \\ C_{21} & C_{22} & C_{23} & C_{24} & C_{25} & C_{26} \\ C_{31} & C_{32} & C_{33} & C_{34} & C_{35} & C_{36} \\ C_{41} & C_{42} & C_{43} & C_{44} & C_{45} & C_{46} \\ C_{51} & C_{52} & C_{53} & C_{54} & C_{55} & C_{56} \\ C_{61} & C_{62} & C_{63} & C_{64} & C_{65} & C_{66} \end{bmatrix} \begin{bmatrix} \varepsilon_{xx} \\ \varepsilon_{yy} \\ \varepsilon_{zz} \\ \gamma_{yz} \\ \gamma_{xz} \\ \gamma_{xy} \end{bmatrix} \tag{1}$$

The stiffness tensor C_{ij} is defined by the local elastic property and orientation. The strain tensor can be computed using displacements in the three principle directions (*x*-*y*-*z*):

$$\begin{bmatrix} \varepsilon_{xx} \\ \varepsilon_{yy} \\ \varepsilon_{zz} \\ \gamma_{yz} \\ \gamma_{xz} \\ \gamma_{xy} \end{bmatrix} = \begin{bmatrix} \frac{\partial u_x}{\partial x} \\ \frac{\partial u_y}{\partial y} \\ 0 \\ \frac{\partial u_z}{\partial y} \\ \frac{\partial u_z}{\partial x} \\ \frac{\partial u_x}{\partial y} + \frac{\partial u_y}{\partial x} \end{bmatrix} \tag{2}$$

As the crystals' geometry in *z* direction is not available on the EBSD section, we consider the wave to propagate only in *x*-*y* plane and the wave-front is planar in *z* direction. The wavefront can be curved in the *x*-*y* plane. In this case, all the partial derivatives of displacement with respect to *z* ($\frac{\partial u_i}{\partial z}$) are zero. The momentum balance equations are expressed as:

$$\begin{cases} \frac{\partial \sigma_{xx}}{\partial x} + \frac{\partial \sigma_{xy}}{\partial y} = \rho \ddot{u}_x \\ \frac{\partial \sigma_{xy}}{\partial x} + \frac{\partial \sigma_{yy}}{\partial y} = \rho \ddot{u}_y \\ \frac{\partial \sigma_{xz}}{\partial x} + \frac{\partial \sigma_{yz}}{\partial y} = \rho \ddot{u}_z \end{cases} \tag{3}$$

where $\ddot{u}_i$ is the second derivative of u_i with respect to time (i.e., acceleration). It is noted that although the modelling domain is 2D, three displacements and accelerations are calculated due to the anisotropy effect. Considering the wave to propagate in the *x*-*y* plane, shear wave splitting can also be modelled with displacements in both the x-*y* plane and in *z* direction. Because we assume a plane wave in *z* direction, the partial derivatives of stress with respect to *z* are assumed to be zero. Eq. (2) can be substituted into Eq. (1) to express stress as a function of displacement, and the result can be substituted into Eq. (3) to form a closed system of three equations for three unknowns (u_x, u_y and u_z).

2.2. Rotation of stiffness tensor

The stiffness tensor C_{ij} depends on the local mineralogy and crystallographic orientation. At each pixel in the EBSD data, the Euler angles following the Bunge convention (ϕ_1, Φ, ϕ_2 in the order of *z*-*x*-*z* rotation) are available to characterize the orientation of the crystal (Bunge, 1993). The stiffness tensor at every pixel must be rotated according to these Euler angles. The 4th order tensor rotation is expressed as:

$$C^R_{ijkl} = R_{im} R_{jn} R_{ko} R_{lp} C_{mnop} \tag{4}$$

where the Einstein summation is used, C_{mnop} is the original 4th rank stiffness tensor defined in the sample coordinate system, and C^R_{ijkl} is the rotated stiffness tensor in the crystal coordinate system (Fig. 1). The 4th rank tensor C^R_{ijkl} is equivalent to C_{ij} as defined in Eq. (1) without employing the Voigt notation. In this case, R is the 2nd order rotation matrix defined as:

This rotation matrix is composed of three single rotation matrices ($R = R_1 R_2 R_3$) following the order of *z*-*x*-*z* rotations.

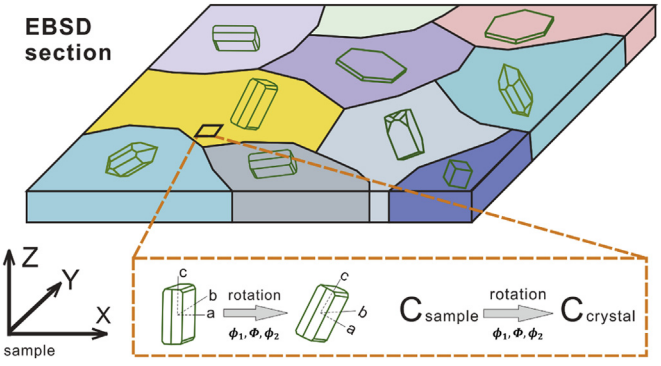

Fig. 1. EBSD section containing crystals with different symmetry and orientation. The zoomed-in pixel schematically shows the rotation of a crystal's stiffness tensor from sample reference frame (a//x, b//y, c//z) to crystal reference frame (actual orientation in rock). The directions of the three axes follow the right-hand rule.

$$R = \begin{bmatrix} \cos(\phi_1)\cos(\phi_2) - \sin(\phi_1)\cos(\Phi)\sin(\phi_2) & -\cos(\phi_1)\sin(\phi_2) - \sin(\phi_1)\cos(\Phi)\cos(\phi_2) & \sin(\phi_1)\sin(\Phi) \\ \sin(\phi_1)\cos(\phi_2) + \cos(\phi_1)\cos(\Phi)\sin(\phi_2) & -\sin(\phi_1)\sin(\phi_2) + \cos(\phi_1)\cos(\Phi)\cos(\phi_2) & -\cos(\phi_1)\sin(\Phi) \\ \sin(\Phi)\sin(\phi_2) & \sin(\Phi)\cos(\phi_2) & \cos(\Phi) \end{bmatrix} \quad (5)$$

$$R_1 = \begin{bmatrix} \cos(\phi_1) & -\sin(\phi_1) & 0 \\ \sin(\phi_1) & \cos(\phi_1) & 0 \\ 0 & 0 & 1 \end{bmatrix} \quad (6)$$

$$R_2 = \begin{bmatrix} 1 & 0 & 0 \\ 0 & \cos(\Phi) & -\sin(\Phi) \\ 0 & \sin(\Phi) & \cos(\Phi) \end{bmatrix} \quad (7)$$

$$R_3 = \begin{bmatrix} \cos(\phi_2) & -\sin(\phi_2) & 0 \\ \sin(\phi_2) & \cos(\phi_2) & 0 \\ 0 & 0 & 1 \end{bmatrix} \quad (8)$$

The stiffness tensor at every pixel in the EBSD section is computed based on the mineralogy (stiffness tensor in sample reference frame) and crystallographic orientation (Fig. 1). The rotation of the stiffness tensors places them into their actual orientation based on the EBSD measurements. Direct FD-simulation can thus be performed on the digital EBSD section detailed in the next section.

2.3. Numerical FD stencil

The FD model is built with a staggered-grid stencil (Fig. 2). FD discretization is applied for both time (explicit) and space (Frehner et al., 2008). The density, displacement and acceleration are located on the nodal points (yellow dots in Fig. 2). The crystallographic orientations measured by EBSD, and hence the stiffness tensors, are located at the center of each element (blue boxes in Fig. 2) surrounded by four nodal points. According to Krüger et al. (2005), the stiffness tensor C_{ij} located at the center of an element must only correspond to one of the neighboring media at grain boundaries and must not be averaged. This is advantageous for EBSD-based wave propagation simulations because the positions of the stiffness tensor naturally coincide with EBSD measurements, which are done in a square grid, and no spatial averaging is needed. Thus, no special treatment on grain boundaries is required. In case the modelling domain is rotated, all the physical properties on the rotated domain are found based on the nearest neighbor on the original unrotated domain.

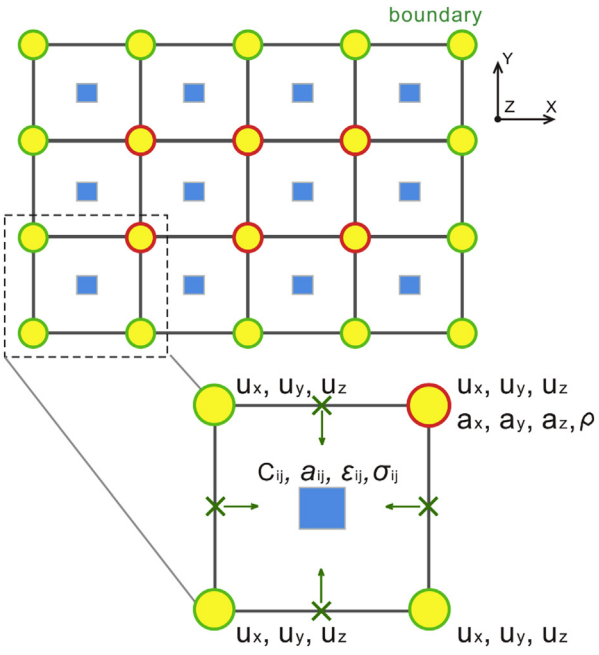

Fig. 2. Finite difference stencil. Blue boxes (element center) correspond to the locations of EBSD measurements and hence stiffness tensors. All displacements, u_i, and accelerations, a_i, are located on the nodal points (yellow dots). For nodal points, green circles indicate boundary conditions and red circles indicate where displacements are updated every explicit time step. Spatial derivatives of displacements are calculated at positions marked by green crosses. These derivatives are arithmetically averaged to place strain at the element center following the green arrows. (For interpretation of the references to color in this figure legend, the reader is referred to the Web version of this article.)

Because density is assigned according to the indexed mineral phases, arithmetic averaging is required to move density from the EBSD measurement points (center of each element; blue boxes in Fig. 2) to the nodal points (yellow dots in Fig. 2; except at boundary nodes). In each explicit FD time step, the strains and stresses are also arithmetically averaged to coincide with the positions of the stiffness tensor for using Hooke's law (Eq. (1)) (Frehner, 2009, Appendix B). The arithmetic averaging for strain is shown in Fig. 2. The computer program is fully vectorized to save computation time.

To ensure numerical stability in the explicit FD time-marching technique, the von Neumann stability criterion is used, where the time increment is a function of grid distance divided by the maximal P-wave velocity ($V_{p,max}$) (Virieux, 1986; Bohlen and Saenger, 2006). The program automatically searches for $V_{p,max}$ among all the present phases based on the given stiffness tensors. The computed explicit time increment is further divided by 4 to increase numerical accuracy. Initially, a Ricker wavelet is applied to the left edge of the model that propagates toward the right edge of the model. The displacement is expressed as:

$$u_i = A\left(1 - \frac{x^2}{l^2}\right)\exp\left(-\frac{x^2}{2l^2}\right) \quad (9)$$

where A is a pre-factor, l is the input dominant wavelength (the dominant frequency is $V/\sqrt{2}\pi l$). Neumann boundary conditions are applied for all displacement components around the modelling domain. Practically, the displacements at the nodal points on the boundary of the modelling domain are updated explicitly based on their interior neighbors in each time step. Seismic waves will be reflected when encountering the boundaries of the EBSD section. The input elastic energy is thus not dissipated at the boundary since no absorbing boundary conditions are defined.

3. *E*-Wave program

A MATLAB program (*E*-Wave) is provided here to directly perform dynamic wave propagation simulations on a measured EBSD section. The *E*-Wave program interface is shown in Fig. 3A. The code uses the built-in functionality of the MATLAB graphic user interface (GUI). The program is named *EWave.exe* and can be executed on Windows computers with a double click. Before executing the code, MATLAB 2017 and Microsoft Excel software (for data import) must be pre-installed. If MATLAB license is not available, users are recommended to visit the MathWorks Web site (http://www.mathworks.com/products/compiler/mcr/index.html) to download the free MATLAB Runtime version 9.2, 64-bit. This allows users to execute the *E*-Wave program without a full MATLAB installation.

3.1. Data import

The EBSD data for the *E*-Wave program is saved in a Microsoft Excel file following the example template (sample ZAP205) in the

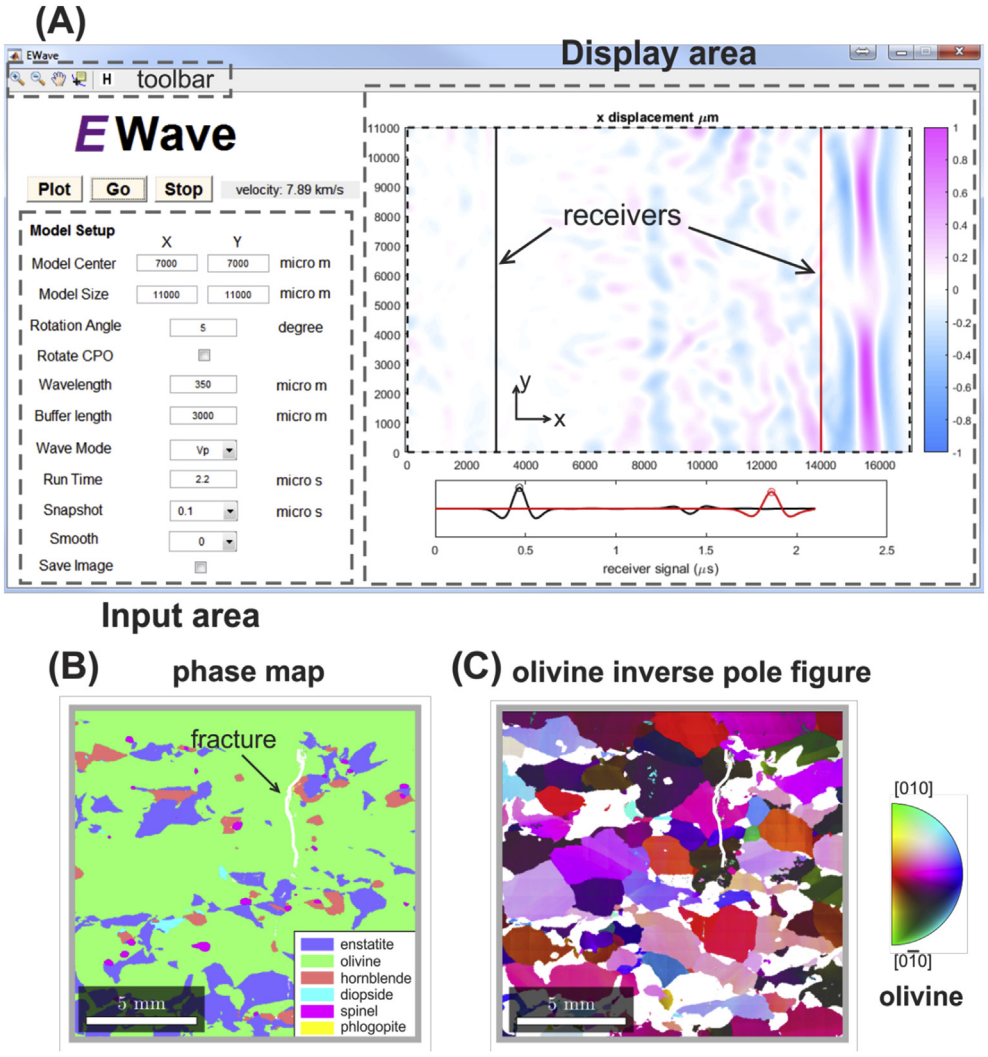

Fig. 3. (A) *E*-Wave program interface. The left panel is the input area to set up model parameters and the right panel is the display area. The example shows wave propagation through a 2D EBSD section of sample ZAP205 from Finero peridotite, Italy (Zhong et al., 2015). The toolbar contains zoom-in, zoom-out, pan, and data selection. The "H" button leads to the help menu. **(B)** Mineral phases of the used sample ZAP205. A fracture is oriented perpendicular to the wave propagation direction. **(C)** Olivine inverse pole figure. MTEX toolbox 4.5.0 is used for plotting the phase map and the inverse pole figure (Mainprice et al., 2011).

supplementary materials (*data.xlsx*). For illustration purposes, only 15 pixels are shown in Fig. 4. The required information includes the *x*-*y* spatial coordinates of each pixel in micrometer, the Euler angles following Bunge convention (*z*-*x*-*z* rotation) in radian, and the phase index given as integers starting from zero (zero is often defined as non-indexed phase). The stiffness tensor and density of each phase are saved in individual spreadsheets with names corresponding to the phase index (Fig. 4). The density and stiffness tensor must be filled in the colored area in each spreadsheet (Fig. 4) for all the phases present in the EBSD data. Thereby, the stiffness tensor has to be written as C_{ij} using the Voigt notation (see Equation (1)).

One potential data import problem occurs when MATLAB attempts to load an Excel file with Microsoft Office language setting other than English. Even though the data format is correct, a "Data loading error" may occur. To fix this problem, in the Excel software go to "*File*", open "*Options*", then "*Add-ins*", select the "*Manage: COM Add-ins*", and uncheck all the items. Meanwhile, the directory to save the software must be set in English for successful execution.

3.2. Input area

The *E*-Wave program can be executed with a double click on the *EWave.exe* icon. Once started, click the "Import Data" button and choose the Excel data file. When the data is loaded, the phase map will be plotted on the screen. The model parameters need to be defined:

- *Model Center*: The *x*-*y* coordinates of the center of the rectangular modelling domain. It must be within the EBSD data domain as shown after data import.
- *Model Size*: The width and height (in *x* and *y* directions) of the rectangular modelling domain. The size must be chosen so that the modelling domain is within the EBSD data domain even after rotation of the modelling domain (see point below).
- *Rotation Angle:* The clockwise rotation angle of the rectangular modelling domain. If left empty, the rotation angle is set to zero by default. Users can systematically vary this value to change the direction of the incident seismic wave, which always propagates from the left to the right side of the rectangular modelling domain.
- *Rotate CPO*: Not only the shape orientations of grains are rotated; the crystallographic orientations of the grains also need to be rotated. Check this box to ensure that the crystallographic orientations of all the pixels are rotated following the "*Rotation Angle*". Uncheck this box to keep all the crystallographic orientations fixed as given by the original Euler angles in the EBSD data. By comparing the seismic velocity as a function of rotation angle with and without checking this box, users can separate the influence of CPO and SPO

(A)

	A	B	C	D	E	F
1	Coordinate (micro m)		Bunge Angle (radian)			Phase
2	X	Y	phi1	psi	phi2	index
3	0	0	1.23	2.12	0.05	1
4	25	0	3.14	3.14	3.14	0
5	50	0	0.41	1.25	0.4	2
6	75	0	2.61	0.15	2.83	2
7	100	0	1.74	2.71	2.87	3
8	0	25	1.65	2.83	1.73	1
9	25	25	0.43	1.47	0.18	2
10	50	25	0.72	1.17	1.95	4
11	75	25	0.72	1.17	1.95	4
12	100	25	0.72	1.17	1.95	4
13	0	50	2.23	1.53	1.41	5
14	25	50	0.57	2.45	0.69	2
15	50	50	2.23	1.53	1.41	1
16	75	50	3.14	3.14	3.14	0
17	100	50	3.14	3.14	3.14	0
18						

(B)

	A	B	C	D	E	F	G
1	Phase 1						
2	Rho (kg/m3)	3369					
3	Stiffness Tensor (GPa)	231	78.9	61.4	0	0	0
4		78.9	169.8	49.1	0	0	0
5		61.4	49.1	215.7	0	0	0
6		0	0	0	82.8	0	0
7		0	0	0	0	76.5	0
8		0	0	0	0	0	78.1

Fig. 4. Example of *E*-Wave program data file. **(A)** EBSD data format. The x-y coordinates follow the 2D EBSD scanning order. There is no need to differentiate either x or y coordinate increases first. **(B)** Physical parameter format. The density (Rho) is in light green and the stiffness tensor in blue following the Voigt notation (see section 2.1). All the existing phases in **(A)** must be present in a separate spreadsheet containing their corresponding physical parameters. (For interpretation of the references to color in this figure legend, the reader is referred to the Web version of this article.)

on seismic anisotropy.

- *Wavelength:* The wavelength of the incident Ricker wavelet (see Eq. (9)). By systematically varying this value, users can investigate how seismic anisotropy is influenced by the incident wavelength (or equivalently the dominant frequency).
- *Buffer length*: In order to guarantee a smooth source wave and avoid disturbance from the boundary, two virtual aluminum "buffers" are attached to both the left and right sides of the modelling domain. This parameter controls the length in x direction of the buffers.
- *Wave Mode*: Define the initial displacement direction. V_p for displacement in x direction (resulting in a P-wave), V_{s1} for y direction (resulting in an S-wave polarized parallel to the y axis, i.e. within the EBSD section) and V_{s2} for z direction (resulting in an S-wave polarized parallel to the z axis, i.e., in and out of the EBSD section).
- *Run Time*: The total running time of the model in microseconds. If this box is left empty, the model will continue running until the "*Stop*" button is clicked.
- *Snapshot:* Choose the time interval in microseconds to plot the displacement field in the display area. The number of time increments per snapshot is rounded; so the actual time interval may not be exactly equal to the chosen value.
- *Smooth:* In case of sharp contrasts in elastic constants and density at grain boundaries, numerical instability may occur that causes the model to fail after a long propagation time. The *Smooth* function allows the user to replace the elastic constants and density at each grid by the arithmetic mean of the neighboring four grids. The default is set as "0" to switch it off. By increasing the number of smoothing, the above procedure is repeated.
- *Save Image*: Check this box to output the displacement field as . *jpg* file for every snapshot. A wave propagation animation can be produced using the exported images.

After data import, three buttons will appear:

- *Plot*: Click this button to visualize the EBSD phase map and the rectangular modelling domain set by the parameters above. A runtime suggestion is displayed once this button is clicked. Depending on the chosen wave mode, this time suggestion is derived using the averaged bulk or shear modulus to compute seismic velocity assuming isotropic elasticity for all mineral phases. The displayed time suggestion can help users to find a rough estimate of when the wavefront reaches the right receiver (a factor of 1.25 is multiplied to guarantee that the wave can pass through the right receiver after the time suggestion).
- *Go*: Click this button to start the numerical simulation of dynamic wave propagation.
- *Stop*: The simulation stops if 1) "*Run Time*" is reached or 2) this "*Stop*" button is clicked. Once stopped, the seismic velocity will be displayed. The velocity is computed using the model length and the time interval between the maximal displacement recorded by the

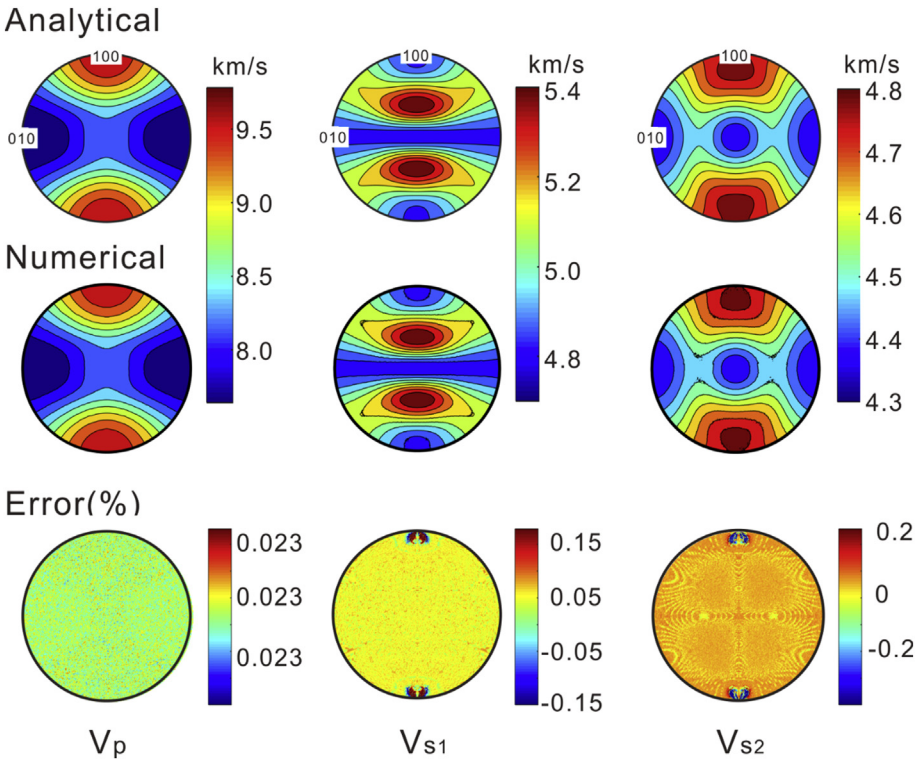

Fig. 5. Benchmark results of a single olivine crystal for seismic velocity. The top row shows analytical solutions computed with the Christoffel tensor and the middle row shows numerical solutions computed with the *E*-Wave model. The bottom row shows the error in percent ($\frac{v_{ana} - v_{num}}{v_{ana}} \times 100$) where v_{ana} is the analytical solution and v_{num} is the numerical solution. In order to achieve sufficient grid resolution for the stereonet projection, 90000 rotations are calculated using the Euler supercomputer cluster in Lugano, Switzerland.

left and right receivers (solid black and red lines in Fig. 3). Users can also manually select the arrival time of seismic wave using the zoom-in and data selection functions in the toolbar (Fig. 3). After clicking "*Stop*" or "*Run Time*" is reached, a. txt file called "result.txt" is produced containing three columns listing time, and the left and right receiver time signals for users to post-process the results in their software of choice. The two receiver time signals correspond to the arithmetic average of the displacement along the entire left and right receiver lines, respectively.

Once the simulation is stopped, users can modify the model parameter and start another simulation without restarting the program.

3.3. Display area

The display area contains two plot regions (Fig. 3).

- *Top plot*: When EBSD data is imported, the phase map will be visualized here with a colorbar indicating the phase index. After setting the model parameters (e.g. model size, rotation angle), click the "*Plot*" button to visualize the modelling domain. During numerical simulations after clicking the "*Go*" button, the displacement field will be visualized simultaneously. The pink-to-blue colorbar indicates the amplitude of the corresponding displacement depending on the selected wave mode (x displacement for V_p, y displacement for V_{s1} and z displacement for V_{s2}).
- *Bottom plot*: The displacement signal is visualized for both the left and right receivers denoted by black and red color, respectively. The arithmetic average of the corresponding displacement is calculated along the two receiver lines.

4. Benchmarks

Two numerical benchmarks are performed: 1) wave propagation through a single olivine crystal and 2) wave propagation through two periodically stacked isotropic layers.

4.1. Benchmark for single crystal

Olivine is a common anisotropic mineral in the upper mantle that has orthorhombic symmetry. In this benchmark, the elastic stiffness tensor of olivine is rotated systematically covering a discretized hemisphere and the *E*-Wave model simulates seismic waves propagating in each rotation direction. The resulting V_p, V_{s1} and V_{s2} are projected onto equal-angle stereonets and compared to the analytical solutions computed using the Christoffel tensor (Christoffel, 1877). The Christoffel tensor in this benchmark is computed with the MTEX toolbox 4.5.0 in MATLAB (Mainprice et al., 2011, see Appendix). The applied stiffness tensor for the single olivine crystal (Fo_{90}) is taken from Abramson et al. (1997).

The benchmark results (Fig. 5) show that the analytical and numerical solutions of seismic velocity match very well in terms of the velocity patterns in the stereonets. The numerical error in percent is defined as $\frac{v_{num} - v_{ana}}{v_{ana}} \times 100$, where v_{ana} is the analytical solution and v_{num} is the numerical solution. The error is $< 0.2\%$ for all three seismic wave modes. The grid resolution is 5000 in x direction and 10 in y direction to save computation time because the displacements do not vary in y direction. This benchmark suggests that the rotation of the crystallographic orientation is correct, and the accuracy of the numerical solution is sufficient to capture the seismic anisotropy of a single crystal.

4.2. Benchmark for layered rock

The model setup of the second benchmark is a periodically stacked

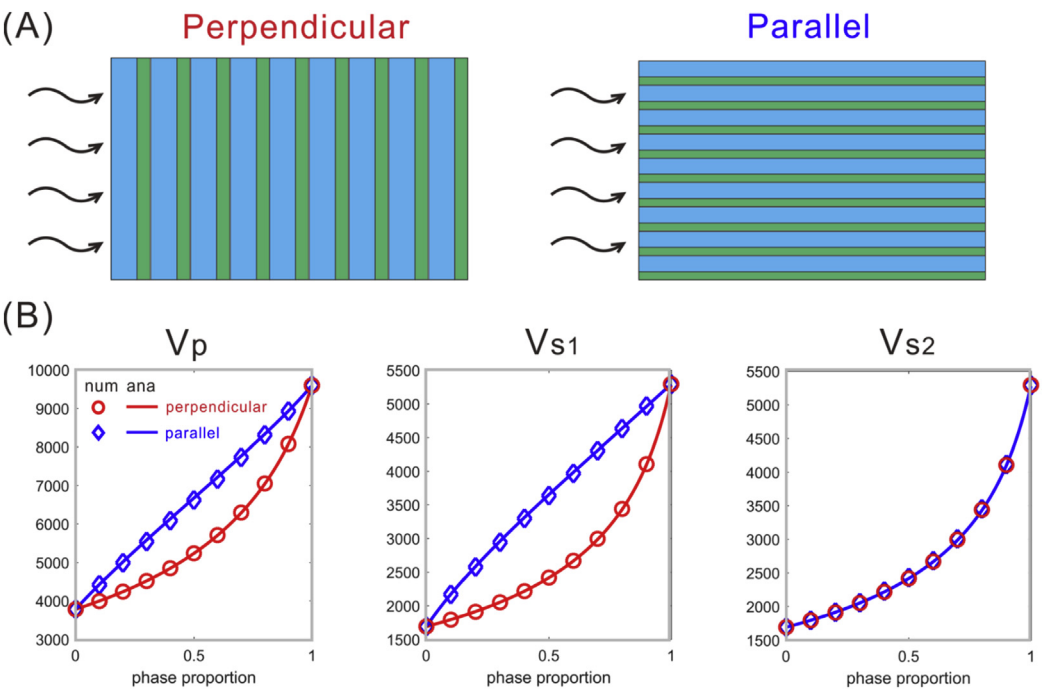

Fig. 6. Benchmark for two periodically layered rocks. The physical properties are tabulated in Table 1. **(A)** Schematic model setup for waves propagating perpendicular (red) or parallel (blue) to the layering. **(B)** Results of seismic velocity as a function of phase proportion of phase one. The numerical solutions (num) are denoted by open circles and diamonds using the *E*-Wave model. The analytical solution (ana) of Backus (1962) is denoted by solid lines. (For interpretation of the references to color in this figure legend, the reader is referred to the Web version of this article.)

Table 1
Phase properties for benchmark model. Both phases are isotropic. The stiffness tensor is computed using the first and second Lamé constants, λ and μ, respectively. The phase colors correspond to the periodic layers in Fig. 6.

	Phase-one (blue)	*Phase-two (green)*
λ	70 GPa	10 GPa
μ	90 GPa	30 GPa
ρ	2500 kg/m^3	3500 kg/m^3

medium with two types of isotropic layers (Fig. 6). In this case, the medium macroscopically behaves transversely isotropic (Backus, 1962). The stiffness tensor for the effective medium can be arithmetically averaged following the Backus solution provided in the Appendix. The seismic wave velocity in different directions can thus be computed using the Backus solution.

Here, the numerical benchmark is performed in this model setup by propagating seismic waves either parallel or perpendicular to the layers (Fig. 6). The two isotropic layers (phase-one and phase-two) have physical properties listed in Table 1. The wavelength of the incident Ricker wavelet is at least 10 times longer than the thickness of the periodic layers to ensure that no significant reflections occur during wave propagation. This ratio has been tested by Arntsen (2007) to assure that the resulting seismic velocity does not suffer from observable elastic scattering.

The good match between numerical and analytical solutions in this benchmark shows that the *E*-Wave model can correctly simulate a perfectly layered rock. This implies that SPO can be satisfactorily simulated in our model. Combined with the previous benchmark to testify the crystallographic rotation (for CPO), natural system with heterogeneous and anisotropic mineral aggregates measured by the EBSD technique can be modelled.

5. Concluding remarks

The MATLAB program *E*-Wave is developed that allows EBSD data import, FD numerical simulations of dynamic wave propagation, live result visualization and processing. The complete mechanical formulation and benchmarks are provided for the FD numerical model. The *E*-Wave program is simple to use by EBSD users without background knowledge in numerical programming. A few potential applications of the *E*-Wave program can be: 1) studying the magnitude and origin of seismic anisotropy by rotating the wave propagation direction with or without rotating the CPO, 2) investigating the elastic scattering and frequency influence of incident wave on seismic anisotropy, and 3) quantifying the seismic influences of inclusions and fractures in EBSD sections. *E*-Wave will assist future studies in seismic anisotropy under the prevalent application of the EBSD technique. The *E*-Wave program (and a stand-alone MATLAB script for the FD modelling part) and an example data file for sample ZAP205 (Finero peridotite, Ivrea Verbano zone, Italy) are available on Github (https://github.com/xinzhong0708/EWave.git). Users can directly paste their EBSD data into the Excel template.

Acknowledgement

This work was supported by Swiss National Science Foundation (P2EZP2_172220). K. Kunze and A. Zappone are thanked for discussions and acquiring/processing EBSD data. We thank B. Almqvist, G.E. Lloyd, A.L. Lee and an anonymous reviewer for their careful review that improved the quality of this work. D. Grana and L. Azevedo are acknowledged for their editorial work. XZ thanks L. Hu and S. Chen for testing the *E*-Wave program.

Appendix

A1. Christoffel tensor

The Christoffel equation (Christoffel, 1877) is used to characterize the elastic wave velocity in an anisotropic medium based on the elastic stiffness tensor C_{ijkl}.

$$T_{ik} = C_{ijkl}\,\vec{n_j}\,\vec{n_l} \tag{A1}$$

where $\vec{n_j}$ and $\vec{n_l}$ are the propagation unit vector in Cartesian coordinate frame. The Einstein summation is used here for matrix multiplication. The eigenvalues ($\lambda_1,\ \lambda_2,\ \lambda_3$) of the Christoffel tensor are related to the three seismic wave velocities:

$$\begin{aligned} V_P &= \sqrt{\lambda_1/\rho} \\ V_{s1} &= \sqrt{\lambda_2/\rho} \\ V_{s2} &= \sqrt{\lambda_3/\rho} \end{aligned} \tag{A2}$$

Therefore, V_p, V_{s1}, and V_{s2} are obtained for a single crystal in any arbitrary direction. In the benchmark, the Christoffel tensor is computed with the MATLAB MTEX toolbox 4.5.0 (Mainprice et al., 2011).

A2. Backus solution for isotropic layers

The Backus average describes the effective stiffness tensor expressed as below (Backus, 1962):

$$\begin{aligned} A &= \frac{4\mu(\lambda+\mu)}{\lambda+2\mu} + \left\langle \frac{1}{\lambda+2\mu} \right\rangle^{-1} \left\langle \frac{\lambda}{\lambda+2\mu} \right\rangle^{2} \\ B &= \frac{2\lambda\mu}{\lambda+2\mu} + \left\langle \frac{1}{\lambda+2\mu} \right\rangle^{-1} \left\langle \frac{\lambda}{\lambda+2\mu} \right\rangle^{2} \\ C &= \left\langle \frac{1}{\lambda+2\mu} \right\rangle^{-1} \\ D &= \left\langle \frac{1}{\mu} \right\rangle^{-1} \\ F &= \left\langle \frac{1}{\lambda+2\mu} \right\rangle^{-1} \left\langle \frac{\lambda}{\lambda+2\mu} \right\rangle \\ M &= \mu \end{aligned} \tag{A3}$$

where λ and μ are the first and second Lamé constants, $\langle\ \rangle$ indicates the averages of the enclosed properties, weighted arithmetically by the volumetric proportions. The stiffness tensor writes:

$$C_{ij}^{Backus} = \begin{bmatrix} A & B & F & 0 & 0 & 0 \\ B & A & F & 0 & 0 & 0 \\ F & F & C & 0 & 0 & 0 \\ 0 & 0 & 0 & D & 0 & 0 \\ 0 & 0 & 0 & 0 & D & 0 \\ 0 & 0 & 0 & 0 & 0 & M \end{bmatrix} \tag{A4}$$

Therefore, the seismic wave velocity can be computed with C_{ij}^{Backus} in different directions, either parallel ([100], [010]) or perpendicular ([001]) to the layering.

References

Abramson, E.H., Brown, M., Slutsky, L.J., Zaug, J., 1997. The elastic constants of San Carlos olivine to 17 GPa. J. Geophys. Res. 102, 12252–12263. https://doi.org/10.1029/97JB00682.

Adams, B.L., Wright, S.I., Kunze, K., 1993. Orientation imaging: the emergence of a new microscopy. Metall. Trans. A 24, 819–831. https://doi.org/10.1007/BF02656503.

Almqvist, B.S.G., Mainprice, D., 2017. Seismic properties and anisotropy of the continental crust: predictions based on mineral texture and rock microstructure. Rev. Geophys. 55, 367–433. https://doi.org/10.1002/2016RG000552.

Anderson, D., Minster, B., Cole, D., 1974. The effect of oriented cracks on seismic velocities. J. Geophys. Res. 79, 4011–4015.

Arntsen, B., 2007. Validity of the long-wave approximation in layered media. Geophys. Prospect. 55, 49–56.

Austrheim, H., Dunkel, K.G., Plümper, O., Ildefonse, B., 2017. Fragmentation of wall rock garnets during deep crustal earthquakes. Sci. Adv 3, 1–8.

Backus, G.E., 1962. Long-wave elastic anisotropy produced by horizontal layering. J. Geol. 67, 4427–4440.

Bascou, J., Barruol, G., Mainprice, D., Egydio-Silva, M., 2001. EBSD-measured lattice-preferred orientations and seismic properties of eclogites. Tectonophysics 342, 61–80.

Bohlen, T., Saenger, E.H., 2006. Accuracy of heterogeneous staggered-grid finite-difference modeling of Rayleigh waves. Geophysics 71, T109. https://doi.org/10.1190/1.2213051.

Brown, J.M., 2015. Determination of Hashin-Shtrikman bounds on the isotropic effective elastic moduli of polycrystals of any symmetry. Comput. Geosci. 80, 95–99. https://doi.org/10.1016/j.cageo.2015.03.009.

Bunge, H.J., 1993. Texture Analysis in Materials Science: Mathematical Methods. Elsevier. https://doi.org/9781483278391.

Christoffel, E.B., 1877. Über die Fortpflanzung von Stössen durch elastiche feste Körper. Ann.. di Mat. Pura ed Appl 8, 193–243.

Dunkel, K.G., Austrheim, H., Renard, F., Cordonnier, B., Jamtveit, B., 2017. Localized slip controlled by dehydration embrittlement of partly serpentinized dunites, Leka Ophiolite Complex. Norway. Earth Planet. Sci. Lett. 463, 277–285. https://doi.org/10.1016/j.epsl.2017.01.047.

Frehner, M., 2009. Numerical Modeling of Multiscale Wave Propagation Phenomena in Fluid–rock Systems. ETH Zurich, Switzerland.

Frehner, M., Schmalholz, S.M., Saenger, E.H., Steeb, H., 2008. Comparison of finite difference and finite element methods for simulating two-dimensional scattering of elastic waves. Phys. Earth Planet. In. 171, 112–121. https://doi.org/10.1016/j.pepi.2008.07.003.

Hill, R., 1952. The elastic behaviour of a crystalline aggregate. Proc. Phys. Soc. 65, 349–354.

Humphreys, F.J., 2001. Grain and subgrains characterisation by electron backscatter diffraction. J. Mater. Sci. 36, 3833–3854. https://doi.org/10.1023/A:1017973432592.

Kneller, E.A., van Keken, P.E., 2007. Trench-parallel flow and seismic anisotropy in the Mariana and Andean subduction systems. Nature 450, 1222–1225. https://doi.org/10.1038/nature06429.

Krüger, O.S., Saenger, E.H., Shapiro, S.A., 2005. Scattering and diffraction by a single crack: an accuracy analysis of the rotated staggered grid. Geophys. J. Int. 162, 25–31. https://doi.org/10.1111/j.1365-246X.2005.02647.x.

Lloyd, G.E., Halliday, J.M., Butler, R.W.H., Casey, M., Kendall, J.-M., Wookey, J., Mainprice, D., 2011. From crystal to crustal: petrofabric-derived seismic modelling of regional tectonics. Geol. Soc. London, Spec. Publ. 360, 49–78. https://doi.org/10.1144/SP360.4.

Long, M.D., Becker, T.W., 2010. Mantle dynamics and seismic anisotropy. Earth Planet Sci. Lett. 297, 341–354. https://doi.org/10.1016/j.epsl.2010.06.036.

Mainprice, D., 2015. Seismic Anisotropy of the Deep Earth from a Mineral and Rock Physics Perspective, Treatise on Geophysics. Elsevier B.V. https://doi.org/10.1016/B978-044452748-6.00045-6.

Mainprice, D., Hielscher, R., Schaeben, H., 2011. Calculating anisotropic physical properties from texture data using the MTEX open-source package. Geol. Soc. London, Spec. Publ. 360, 175–192. https://doi.org/10.1144/SP360.10.

Mavko, G., Mukerji, T., Dvorkin, J., 2009. The Rock Physics Handbook : Tools for Seismic Analysis of Porous Media.

Naus-Thijssen, F.M.J., Goupee, A.J., Johnson, S.E., Vel, S.S., Gerbi, C., 2011. The influence of crenulation cleavage development on the bulk elastic and seismic properties of phyllosilicate-rich rocks. Earth Planet Sci. Lett. 311, 212–224. https://doi.org/10.1016/j.epsl.2011.08.048.

Schoenberg, M., 1995. Seismic anisotropy of fractured rock. Geophysics 60 (204).

https://doi.org/10.1190/1.1443748.
Schoenberg, M., Muirt, F., 1989. A calculus for finely layered anisotropic media. Geophysics 54, 581–589.
Skemer, P., Hansen, L.N., 2016. Inferring upper-mantle flow from seismic anisotropy: an experimental perspective. Tectonophysics 668–669, 1–14. https://doi.org/10.1016/j.tecto.2015.12.003.
Vel, S.S., Cook, A.C., Johnson, S.E., Gerbi, C., 2016. Computational homogenization and micromechanical analysis of textured polycrystalline materials. Comput. Meth. Appl. Mech. Eng. 310, 749–779. https://doi.org/10.1016/j.cma.2016.07.037.
Virieux, J., 1986. P-SV wave propagation in heterogeneous media: velocity-stress finite-difference method. Geophysics 51, 889–901.
Willis, J.R., 1977. Bounds and self-consistent estimates for the overall properties of nonlinear composites. J. Mech. Phys. Solid. 25, 185–202. https://doi.org/10.1093/imamat/39.3.215.
Zhong, X., Frehner, M., Kunze, K., Zappone, A., 2014. A novel EBSD-based finite-element wave propagation model for investigating seismic anisotropy: application to Finero Peridotite, Ivrea-Verbano Zone. Northern Italy. Geophys. Res. Lett. 41, 7105–7114. https://doi.org/10.1002/2014GL060490.Received.
Zhong, X., Frehner, M., Zappone, A., Kunze, K., 2015. A numerical and experimental investigation on seismic anisotropy of. IOP Conf. Ser. Mater. Sci. Eng. 82 (12072). https://doi.org/10.1088/1757-899X/82/1/012072.